# An On-site Current Profile Estimation Algorithm for a Moored Floating Structure ⋆

**Zhengru Ren** [*,**] **Roger Skjetne** [*,**]

[*] *Centre for Research-based Innovation on Marine Operations (SFI MOVE), Department of Marine Technology, Norwegian University of Science and Technology, NTNU, NO-7491 Trondheim, Norway, (e-mail: zhengru.ren@ntnu.no, roger.skjetne@ntnu.no)*
[**] *Centre for Autonomous Marine Operations and Systems (AMOS), Department of Marine Technology, Norwegian University of Science and Technology, NTNU, NO-7491 Trondheim, Norway*

**Abstract:** The current speed influences the safety of subsea and marine operations. This paper proposes an algorithm to estimate the depth-dependent current profile though data from existing commercial sensors, that is the mooring line tension measurements and riser end angle measurements. This will aid prediction of the weather window to enhance the safety during the subsea operations. The influence of various current profile types and the vessel's motion are discussed. A governing equation is proposed for the algorithm. A simulation is conducted to verify the algorithm.

*Keywords:* Current profile estimation, moored structure, subsea operation.

## 1 Introduction

The weather window is determined to ensure the safety of a marine operation. For instance, the payload position is not observable during the deep water lifting operation. The underwater robots also benefit from the current profile, which ensures safe operation. The full current profile over depth is driven by the wind, the tide, and the ocean current. Regarding the wind generated current, it mainly functions in the shallow water region near the water surface, while its influence lessens with the increase of the water depth. The surface current component generated by the local wind is approximately proportional to the wind velocity. The depth dependence of tidal and local wind components are functions of the water depth and the velocity components at the water surface (Faltinsen, 1993). However, it is unrealistic to separate one component from the others. Various commercial sensors can be applied to detect the current speed at a specific location, such as the acoustic Doppler current meter, the electromagnetic current meter, the tilting current meter, and the cameras (Antonelli et al., 2008). As the current speed is neither spatially nor temporally uniform along the depth, multiple current meters are needed in such scenario. Additionally, these sensors must be installed, which will be costly.

An on-site current profile estimator has the potential to improve the safety and performance during a marine operation, such as field installation and drilling. The relative motion between water particular and a slender body induces the damping loads, which influence the total loads acting on the risers and the mooring lines. This will influence active riser control. Ren et al. (2015b) and Ren and Skjetne (2016) present several tension-based algorithms to locate a moored vessel. Wind velocity can be measured through wind sensors, and the wave spectrum is available from oceanographic data and onboard systems, for example Nielsen and Jensen (2011). For surface vessels exposed to an environmental disturbance with unknown current speed, Lekkas and Fossen (2014) proposed an approach to estimate the surface current speed with a couple of nonlinear adaptive observers.

⋆ This work was supported by the Research Council of Norway (RCN) through the Centre for Research-based Innovation on Marine Operations (RCN-project 237929), and partly by the Centre of Excellence AMOS (RCN-project 223254).

This paper proposes a deterministic approach to estimate the 2D on-site current profile for a moored structure. All the necessary data come from existing commercial sensors of the winch monitoring systems and the riser management system.

## 2 Problem statement

A floating structure is moored with $m$ mooring lines, and at least one rigid riser is operated. The bottom ends of the mooring lines are the anchors fixed on the seafloor, i.e., $\boldsymbol{p}_a^j = \left[x_a^j \; y_a^j \; z_a^j\right]^\top \in \mathbb{R}^3$, where the superscript $j$ refers to the index of the anchor, $j = 1, \cdots, m$. Each mooring lines is connected to a winch through a fairlead. The corresponding position of the fairlead is $\boldsymbol{p}_f^j = \left[x_f^j \; y_f^j \; z_f^j\right]^\top \in \mathbb{R}^3$. The priori information is the characteristic parameters of the mooring lines and the riser, the precise locations of the anchors and the riser bottom ends during installation, and the key matrices of the moored structure. The winch monitoring system has a tension cell at the end of each cables. Now, we define a set of tension measurements, i.e., $\mathscr{T} = \{T_j | j = 1, \cdots, m\}$. A tensioner with a heave compensator is equipped at the end of each riser to provide a constant top tension $T_{top}$ to increase its stiffness and limit the payoff. The top and bottom end angles of the riser, i.e., $\vartheta = \{\theta_t, \theta_b\}$, are measured.

Suppose the current velocity magnitude is a depth-dependent piecewise continuously surjective function, such that $v_c(t) = f_c(z,t)$, where $f_c : [0, D] \times [0, \infty) \mapsto \mathbb{R}$, where $D$ is the water depth. The current profile is arbitrary, for example the uniform, the linearly shared, the Ormen Lange, the GoM, and the bidirectional seen in Fig. 1. Now we discretize the profile into $p$ discrete segments at a set of specific water depths, i.e., $\mathscr{D} = \{D_h | h = 1, \cdots, p\}$. In Table 1, $v \in \mathbb{R}$ is a variable that defines the profile. Additionally, a current velocity set $\mathscr{V}_c = \{v_c^h | h = 1, \cdots, p\}$ and a current orientations set $\mathscr{B}_c = \{\beta_c^h | h = 1, \cdots, p\}$ contain the magnitudes and directions of the current velocities at the depth $D_h \in \mathscr{D}$, where $h = 1, \cdots, p$, are defined. When $\mathscr{V}_c$ is determined, we can resample the current speed at an arbitrary depth with an interpolation. In this paper, we only consider a 2D distributed current, i.e., $\beta_c^1 \equiv \cdots \equiv \beta_c^p = \beta_c$. This is a simplified condition in the design period. The current directions along the depth are kept in the $x$-$z$ plane, in which

the unknown current direction is $\mathscr{B}_c = \{\beta_c\}$. Therefore, the problem is formed to estimate $(\mathscr{V}_c, \beta_c)$ from $(\mathscr{D}, \mathscr{T}, T_{top}, \vartheta)$. There are $p+1$ unknown parameters in total.

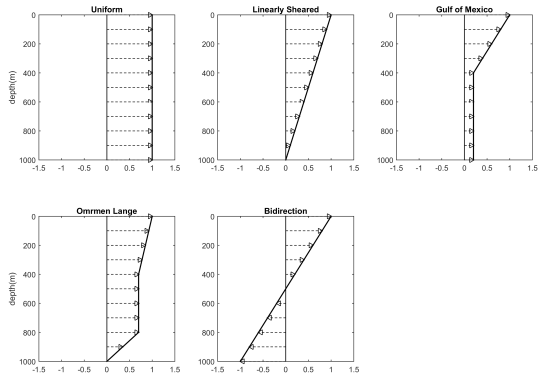


Fig. 1. The bold line in every subfigure is the current profile.

Table 1. Current profile discussed thereafter and their depth-dependent discrete points.

| Type | Depth (m)/Velocity(m/s) | | | |
|---|---|---|---|---|
| Uniform | 0 | 1000 | | |
| | $v$ | $v$ | | |
| Linear | 0 | 1000 | | |
| | $v$ | 0 | | |
| GoM | 0 | 400 | 1000 | |
| | $v$ | $0.2v$ | $0.2v$ | |
| Ormen Lange | 0 | 400 | 800 | 1000 |
| | $v$ | $0.7v$ | $0.7v$ | 0 |
| Bidirectional | 0 | 1000 | | |
| | $v$ | $-v$ | | |

In this paper, we will consider the underwater current profile, while the surface current is disregarded. Consequently, we mainly estimate the current profile below the water surface generated by the current and the tide.

## 3 System modeling

### 3.1 Kinematics

All the 3DOF and 6DOF coordinate systems satisfy the right-hand rule. Five coordinate systems are applied; see Fig. 2.

- The Earth-fixed frame $\{E\}$, denoted as $X_E Y_E Z_E$, is defined as a local north-east-down geographic coordinate.
- The body-fixed frame $\{B\}$, denoted as $XYZ$, refers to the reference frame whose origin coincides with the center of gravity (COG). The positive directions direct from aft to fore along the longitudinal axis of the vessel, starboard, and downward.
- The anchor-fixed frame $\{A_j\}$, denoted as $X_A^j Y_A^j Z_A^j$, is placed at the end of the $j^{th}$ cable. $Z_A^j$ axis points upward. The $X_A^j$ positively directs from the $j^{th}$ anchor to its corresponding fairlead projection on the seafloor.
- The elemental riser frame $\{i\}$, denoted as $\boldsymbol{i}_1\boldsymbol{i}_2\boldsymbol{i}_3$, is placed at a node of the riser, $\boldsymbol{i}_1$ points to the next element, $\boldsymbol{i}_2$ pointing into the plane, and $\boldsymbol{i}_3$ is along the axial direction of the element pointing upwards.
- The local riser-fixed frame $\{f\}$ is fixed at the seafloor pointing positively upward.

Define the 6DOF positions and orientations of the vessel relative to the Earth-fixed frame and the velocity in a body-fixed reference as $\boldsymbol{\eta} = [x\ y\ z\ \phi\ \theta\ \psi]^\top \in \mathbb{R}^6$ and $\boldsymbol{\nu} = [u\ v\ w\ p\ q\ r]^\top \in \mathbb{R}^6$. The relation between them is given by

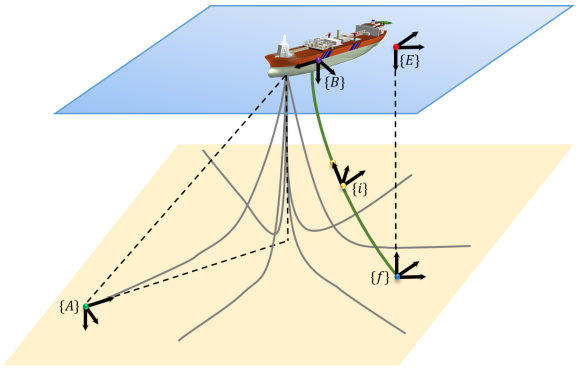


Fig. 2. Current profile.

$$\dot{\boldsymbol{\eta}} = \boldsymbol{J}(\boldsymbol{\eta})\boldsymbol{\nu}, \tag{1}$$

where $\boldsymbol{J}(\boldsymbol{\eta}) = \begin{bmatrix} \boldsymbol{R}(\boldsymbol{\eta}) & \boldsymbol{0}_{3\times3} \\ \boldsymbol{0}_{3\times3} & \boldsymbol{T}(\boldsymbol{\eta}) \end{bmatrix} \in \mathbb{R}^{6\times6}$, $\boldsymbol{R}(\boldsymbol{\eta})$ and $\boldsymbol{T}(\boldsymbol{\eta}) \in \mathbb{R}^{3\times3}$ denote the transformation matrices between the body-fixed frame and the Earth-fixed frame. We also defined a set of angles $\boldsymbol{\Phi}_m$ representing the arrangement of the mooring lines, such that

$$\boldsymbol{\Phi}_m = \{\psi_m^j | \psi_m^j = \tan^{-1}\left(\frac{y - y_a^j}{x - x_a^j}\right),\ j = 1, \cdots, m\}. \tag{2}$$

### 3.2 Kinetics

In what follows, the vessel model described in Fossen (2011) is presented, given by

$$\begin{aligned} \boldsymbol{M}\dot{\boldsymbol{\nu}} + \boldsymbol{C}_{RB}(\boldsymbol{\nu})\boldsymbol{\nu} + \boldsymbol{C}_A(\boldsymbol{\nu}_r)\boldsymbol{\nu}_r + \boldsymbol{D}(\boldsymbol{\nu}_r) \\ = \boldsymbol{\tau}_m + \boldsymbol{\tau}_c + \boldsymbol{\tau}_{wind} + \boldsymbol{\tau}_{wave1} + \boldsymbol{\tau}_{wave2}, \end{aligned} \tag{3}$$

where $\boldsymbol{M} \in \mathbb{R}^{6\times6}$ is the system inertia matrix including the added mass components, $\boldsymbol{C}_{RB}(\boldsymbol{\nu}) \in \mathbb{R}^{6\times6}$ and $\boldsymbol{C}_A(\boldsymbol{\nu}_r) \in \mathbb{R}^{6\times6}$ refer to the skew-symmetric Coriolis and centripetal matrices of the rigid body and the added mass, $\boldsymbol{D}(\boldsymbol{\nu}_r) \in \mathbb{R}^{6\times6}$ denotes the damping matrix, and $\boldsymbol{\tau}_c$, $\boldsymbol{\tau}_{wind}$, $\boldsymbol{\tau}_{wave1}$, and $\boldsymbol{\tau}_{wave2} \in \mathbb{R}^6$ represent the thruster-induced loads, the wind load, and the wave loads, respectively. The mooring load, $\boldsymbol{\tau}_m \in \mathbb{R}^6$, is the sum of restoring forces and moments from all mooring lines, such that $\boldsymbol{\tau}_m = \sum_{j=1}^m \boldsymbol{\tau}_m^j$, where $\boldsymbol{\tau}_m^j$ denotes the force and moment acting on the moored structure generalized from the $j^{th}$ cable. See Fossen (2011) and Sørensen (2012) for details.

### 3.3 FEM model of the mooring lines

The finite element method (FEM) model is developed by Aamo and Fossen (2001). With the proof of the existence and uniqueness of the solution, it can be used to simulate a mooring line in the time domain. The FEM is an accurate modeling method when not considering more complex hydrodynamic effects, such as vertex shedding (Gao and Moan, 2007). The unstretched length of the $j^{th}$ cable is $L^j$. Each of the mooring line is uniformly divided into $n$ segments of length $l^j = L^j/n$, and the weight of all the segments concentrate at all the $n+1$ nodes. From the anchor to the fairlead, the nodes are enumerated from 0 to $n$. When the number of nodes $n$ rises, the model accuracy enhances, but the computational speed reduces. The position vector of the $k^{th}$ node along the $j^{th}$ cable in the Earth-fixed coordinate is symbolically expressed as $\boldsymbol{r}_k^j \in \mathbb{R}^3$. The positions of the bottom and top end nodes are the anchors and the fairleads. A node is only influenced by its nearest neighboring nodes, see Fig. 3. A Galerkin method is then applied to formulate the dynamics of all nodes in the time domain, which is given by

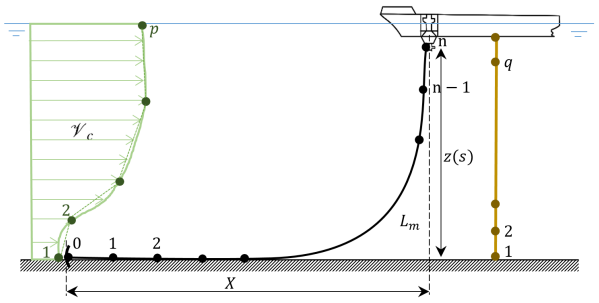


Fig. 3. The FEM models.

$$[\left(\rho_0^j l_j + \frac{C_1^j}{2}(\varepsilon_k^j + \varepsilon_{k+1}^j)\right)\boldsymbol{I}_{3\times3} - \frac{C_1^j}{2}\left(\frac{\boldsymbol{l}_k^j \boldsymbol{l}_k^{j\top}}{\varepsilon_k^j} + \frac{\boldsymbol{l}_{k+1}^j \boldsymbol{l}_{k+1}^{j\top}}{\varepsilon_{k+1}^j}\right)]\ddot{\boldsymbol{r}}_k^i \quad (4)$$
$$= \boldsymbol{f}_{k_{(r)}}^j + \boldsymbol{f}_{k_{(hg)}}^j + \boldsymbol{f}_{k_{(dt)}}^j + \boldsymbol{f}_{k_{(dn)}}^j,\ j = 1,\cdots,m,\ k = 1,\cdots,n-1,$$

where

$$\boldsymbol{l}_k^j = \boldsymbol{r}_k^j - \boldsymbol{r}_{k-1}^j,\ e_k^j = \left|\boldsymbol{l}_k^j\right|/l^j - 1,\ \varepsilon_k^j = |\boldsymbol{l}_k|,\ \boldsymbol{P}_k^j = \boldsymbol{l}_k^j \boldsymbol{l}_k^{j\top}/\varepsilon_k^{j2},$$

$$C_1^j = C_{MN}^j \frac{\pi d_j^2}{4}\rho_w,\ C_2^j = \frac{1}{2}C_{DT}^j d_j \rho_w,\ C_3^j = \frac{1}{2}C_{DN}^j d_j \rho_w,$$

$$\boldsymbol{f}_{k_{(r)}}^j = EA_0^j\left[e_{k+1}^j \boldsymbol{l}_{k+1}^j/\varepsilon_{k+1}^j - e_k^j \boldsymbol{l}_k^j/\varepsilon_k^j\right],$$

$$\boldsymbol{f}_{k_{(hg)}}^j = l^j \rho_0^j \frac{\rho_c^j - \rho_w}{\rho_c^j}[0\ 0\ g]^\top,$$

$$\boldsymbol{f}_{k_{(dt)}}^j = -\frac{C_2^j}{2}\left[\left|\dot{\tilde{\boldsymbol{r}}}_k^j \cdot \boldsymbol{l}_k^j\right|\boldsymbol{P}_k^j + \left|\dot{\tilde{\boldsymbol{r}}}_k^j \cdot \boldsymbol{l}_{k+1}^j\right|\boldsymbol{P}_{k+1}^j\right]\dot{\tilde{\boldsymbol{r}}}_k^j,$$

$$\boldsymbol{f}_{k_{(dn)}}^j = -\frac{C_3^j}{2}\left[\varepsilon_k^j\left|\left(\boldsymbol{I}_{3\times3} - \boldsymbol{P}_k^j\right)\dot{\tilde{\boldsymbol{r}}}_k^j\right|\left(\boldsymbol{I}_{3\times3} - \boldsymbol{P}_k^j\right)\right.$$
$$\left. + \varepsilon_{k+1}^j\left|\left(\boldsymbol{I}_{3\times3} - \boldsymbol{P}_{k+1}^j\right)\dot{\tilde{\boldsymbol{r}}}_k^j\right|\left(\boldsymbol{I}_{3\times3} - \boldsymbol{P}_{k+1}^j\right)\right]\dot{\tilde{\boldsymbol{r}}}_k^j,$$

where the superscript $j$ identifies the $j^{th}$ cable, $\rho_0 = \frac{\pi d^2}{4}(\rho_c - \rho_w)g$ is the mass per unit length of the unstretched cable, $\rho_c$ and $\rho_w$ stand for the cable density and the ambient water density, $d$ denotes the cable diameter, $g$ represents the gravity acceleration, $C_{MN}$ refers to the added mass coefficient, $C_{DT}$ and $C_{DN}$ are the tangential and normal drag coefficients of the cable, $e$ is the strain, $E$ is the Young's modulus of elasticity, $A_0 = \frac{\pi}{4}d^2$ stands for the cross-section area of the unstretched cable, $\boldsymbol{f}_{k_{(hg)}}$, $\boldsymbol{f}_{k_{(r)}}$, $\boldsymbol{f}_{k_{(dt)}}$, and $\boldsymbol{f}_{k_{(dn)}}$ are the buoyancy force, the reaction force, and the tangential and normal hydrodynamic drag per unit length of the unstretched cable, respectively. The top end, i.e., $k = n$, is determined by the motion of the fairlead. The relative surface-fluid velocity in the Earth-fixed reference frame at the depth of the $k^{th}$ node is $\dot{\tilde{\boldsymbol{r}}}_k^j = \dot{\boldsymbol{r}}_k^j - \boldsymbol{v}_{c,k}^j$, where $\boldsymbol{v}_{c,k}^j \in \mathbb{R}^3$ is the current velocity at the depth of the $k^{th}$ node through resampling. The top and bottom restoring forces are then given by

$$\boldsymbol{F}_{top}^j = -EA_0^j \frac{e_n^j}{\varepsilon_n^j}\boldsymbol{l}_n^j \quad \text{and} \quad \boldsymbol{F}_{bot}^j = EA_0^j \frac{e_1^j}{\varepsilon_1^j}\boldsymbol{l}_1^j, \quad (5)$$

and the restoring force and moment vector becomes

$$\boldsymbol{\tau}_m^j = \begin{bmatrix} \boldsymbol{F}_{top}^j \\ \boldsymbol{F}_{top}^j \times (\boldsymbol{p}_f^j - \boldsymbol{p}_{COT}) \end{bmatrix}, \quad (6)$$

where $\boldsymbol{p}_{COT}$ is the position of the center of the turret. The top tension is an $\mathscr{L}_2$ norm of $\boldsymbol{F}_{top}^j$, such that

$$T_j = |\boldsymbol{F}_{top}^j|. \quad (7)$$

In addition to the traditional DP stationkeeping model, which only considers the surge, sway, and yaw motions, the restoring forces at the top ends are additionally influenced by the heave and pitch motion.

### *3.4 2D FEM riser model*

Divide a riser into $q$ segments of length $l_0^r = L^r/q$, where $L^r$ is the length of the riser. Similar to the FEM mooring line model, the nodes, sorted from the seabed to the sea surface, are labeled numerically from 1 to $q$. A tensioner provides a constant top tension $T_{top}$ vertically. The top end of the riser, $z_{r,end}$, is free to move in the vertical direction. Hence, we define a displacement vector,

$$\boldsymbol{r}^r = \left[x_1^r\ z_1^r\ x_2^r\ z_2^r\ \cdots\ x_q^r\ z_q^r\ x\ z_{r,end}\right]^\top. \quad (8)$$

The length and inclination of the $i^{th}$ segment, $l_i^r$ and $\theta_i^r$, are given by $\Delta x_i^r = x_{i+1}^r - x_i^r$, $\Delta z_i^r = z_{i+1}^r - z_i^r$, $l_i^r = \sqrt{\Delta x_i^{r2} + \Delta z_i^{r2}}$, $\cos\theta_i^r = \frac{\Delta z_i^r}{l_i^r}$, and $\sin\theta_i^r = \frac{\Delta x_i^r}{l_i^r}$.

The resulting system dynamics in the global frame is based on a new position vector, i.e., $\boldsymbol{r}^r = [x_1^r z_1^r x_2^r z_2^r \cdots x_q^r z_q^r z_{r,end}]^\top$. The state $x$ is excluded due to the fact that the restoring force at the tensioner is neglected to the upper vessel. The FEM riser model is given by

$$\boldsymbol{M}_r(\boldsymbol{r}_r)\ddot{\boldsymbol{r}}^r + \boldsymbol{C}_r(\boldsymbol{r}^r)\dot{\boldsymbol{r}}^r + \boldsymbol{K}_r(\boldsymbol{r}^r)\boldsymbol{r}^r = \boldsymbol{f}_{top} + \boldsymbol{f}_{cur} - \boldsymbol{f}_{ves}, \quad (9)$$

where $\boldsymbol{M}_r$ is the mass matrix, $\boldsymbol{C}_r$ is the damping matrix, $\boldsymbol{K}_r$ is the stiffness matrix, $\boldsymbol{f}_{top} = [\boldsymbol{0}_{2q}, T_{top}]^\top$ is the tension vector, $\boldsymbol{f}_{cur}$ is the current-induced hydrodynamic load vector, and $\boldsymbol{f}_{ves}$ is the force vector due to vessel motion.

The mass matrix is a sum of structural mass, internal fluid, and hydrodynamic added mass, which is given by

$$\boldsymbol{m}_i^i = \boldsymbol{m}_{si}^r + \boldsymbol{m}_{fi}^r + \boldsymbol{m}_{ai}^r = \frac{\rho_s A l_0^r}{6}\begin{bmatrix}2&0&1&0\\0&2&0&1\\1&0&2&0\\0&1&0&2\end{bmatrix}$$
$$+ \frac{\rho_f A_{int} l_i^r}{6}\begin{bmatrix}2&0&1&0\\0&2&0&1\\1&0&2&0\\0&1&0&2\end{bmatrix} + \frac{\rho_w C_m^r A_e l_i^r}{6}\begin{bmatrix}2&0&1&0\\0&0&0&0\\1&0&2&0\\0&0&0&0\end{bmatrix}, \quad (10)$$

where $\rho_s$ is the density of the riser material, $\rho_f$ is the density of the internal fluid, and $C_m^r$ is the hydrodynamic added mass coefficient. For a cylinder with $C_m^r = 1$, $A$ refers to the cross section area, i.e., $A = \frac{\pi}{4}(d_{ex}^2 - d_{int}^2)$ where $d_{ex}$ and $d_{int}$ are the external and internal diameters of the riser, the internal area is $A_{int} = \frac{\pi}{4}d_{int}^2$, and the external area is $A_{ex} = \frac{\pi}{4}d_{ex}^2$.

In the local reference, the stiffness matrix is a combination of the elastic stiffness $\boldsymbol{k}_E^r$ and the geometric stiffness $\boldsymbol{k}_G^r$, given by

$$\boldsymbol{k}_i^i = \boldsymbol{k}_E^r + \boldsymbol{k}_G^r = \frac{EA}{l_0^r}\begin{bmatrix}0&0&0&0\\0&1&0&-1\\0&0&0&0\\0&-1&0&1\end{bmatrix} + \frac{P_i^r}{l_i^r}\begin{bmatrix}1&0&-1&0\\0&0&0&0\\-1&0&1&0\\0&0&0&0\end{bmatrix} \quad (11)$$

where $P_i^r = \frac{EA}{l_0^r}(l_i^r - l_0^r)$ is the axial tension at the $i^{th}$ node. The geometric stiffness mainly contributes to the lateral resistance (Leira et al., 2011). The mass and stiffness matrices for the $i^{th}$ segment in the global frame are given by

$$\boldsymbol{k}_i^f = \boldsymbol{T}_i^f \boldsymbol{k}_i^i \boldsymbol{T}_i^{f\top} = \begin{bmatrix}\bar{\boldsymbol{k}}_{11}^i & \bar{\boldsymbol{k}}_{12}^i \\ \bar{\boldsymbol{k}}_{21}^i & \bar{\boldsymbol{k}}_{22}^i\end{bmatrix},$$
$$\boldsymbol{m}_i^f = \boldsymbol{T}_i^f \boldsymbol{m}_i^i \boldsymbol{T}_i^{f\top} = \begin{bmatrix}\bar{\boldsymbol{m}}_{11}^i & \bar{\boldsymbol{m}}_{12}^i \\ \bar{\boldsymbol{m}}_{21}^i & \bar{\boldsymbol{m}}_{22}^i\end{bmatrix}, \quad (12)$$

where the transformation matrix for the $i^{th}$ element at both two ends, is

$$\boldsymbol{T}_i^f(\boldsymbol{r}^r) = \begin{bmatrix}\boldsymbol{T}_{0,i}^f(\boldsymbol{r}^r) & \boldsymbol{0}_{2\times2} \\ \boldsymbol{0}_{2\times2} & \boldsymbol{T}_{0,i}^f(\boldsymbol{r}^r)\end{bmatrix}, \quad (13)$$

and the transformation matrix from the local frame to the global frame is given by

$$\boldsymbol{T}_{0,i}^{f}(\boldsymbol{r}^{r}) = \begin{bmatrix} \cos\theta_i^r & \sin\theta_i^r \\ -\sin\theta_i^r & \cos\theta_i^r \end{bmatrix}. \tag{14}$$

The global system mass $\boldsymbol{M}_r$ and stiffness matrix $\boldsymbol{K}_r$ are the matrices without the last second row and column of $\bar{\boldsymbol{M}}_r$ and $\bar{\boldsymbol{K}}_r$, which are given by

$$\bar{\boldsymbol{M}}_r = \begin{bmatrix} \bar{m}_{11}^1 & \bar{m}_{12}^1 & & & & \\ \bar{m}_{21}^1 & \bar{m}_{22}^1+\bar{m}_{11}^2 & \bar{m}_{12}^2 & & & \\ & \bar{m}_{21}^2 & \bar{m}_{22}^2+\bar{m}_{11}^3 & & & \\ & & & \ddots & & \\ & & & & \bar{m}_{22}^{n-1}+\bar{m}_{11}^n & \bar{m}_{12}^n \\ & & & & \bar{m}_{21}^n & \bar{m}_{22}^n \end{bmatrix} \tag{15}$$

and

$$\bar{\boldsymbol{K}}_r = \begin{bmatrix} \bar{k}_{11}^1 & \bar{k}_{12}^1 & & & & \\ \bar{k}_{21}^1 & \bar{k}_{22}^1+\bar{k}_{11}^2 & \bar{k}_{12}^2 & & & \\ & \bar{k}_{21}^2 & \bar{k}_{22}^2+\bar{k}_{11}^3 & & & \\ & & & \ddots & & \\ & & & & \bar{k}_{22}^{n-1}+\bar{k}_{11}^n & \bar{k}_{12}^n \\ & & & & \bar{k}_{21}^n & \bar{k}_{22}^n \end{bmatrix}.$$

The damping matrix is proportional to the mass matrix and the stiffness matrix, that is

$$\boldsymbol{C}_r = \alpha_1 \boldsymbol{M}_r + \alpha_2 \boldsymbol{K}_r \approxeq \alpha_2 \boldsymbol{K}_r, \tag{16}$$

where the coefficient $\alpha_1$ is neglected, and the coefficient $\alpha_2$ is determined by the damping level (Rustad, 2007). Hydrodynamic force is calculated based on the Morison equation, which is applicable to both a mooring line and a riser, given by

$$\boldsymbol{f}_{cur,i} = \int_{z_i^r}^{z_{i+1}^r} \frac{1}{2}\rho_w C_D D_{ex}(\boldsymbol{v}_r - \dot{\boldsymbol{r}}^r)|\boldsymbol{v}_r - \dot{\boldsymbol{r}}^r| dz^r. \tag{17}$$

The riser model is initialized by the quasi-static solution (Rustad, 2007). A 3D slender model can be calculated with commercial software, such as DeepC and SIMA.

### 3.5 *Influence of current direction*

The following two subsections discuss the distinguishability of a current profile from the tension and end angle measurements.

Firstly, we need to analyze the influence of the current direction. The cables are initialized by the catenary equations, where current forces are added to simulate the more realistic situation. The current angle in the simulations of this and the following sections, is in the anchor-fixed frame. The tension variances due to various current velocities and directions are shown in Fig. 4. Hereafter, the number of nodes in the FEM models are set to be 20, which provides both satisfied accuracy and accepted computation efficiency (Rustad, 2007; Aamo and Fossen, 2001).

Due to the page limitation, more results will be illustrated in future works. The quasi-static analysis is conducted with current orientation from 0 to 180 deg. The influence of a current with an orientation in the range of 180 to 360 deg is symmetric. The influence is more notable in the directions, 45 and 135 deg to the projection of the cable on the horizontal plane.

From the results, we find that the influence of a current is approximately proportional to the current magnitude. For a specific type of current profile, the relation between the set of tension measurements $\mathscr{T}$ and current speed $v$ is mathematically one-to-one. Such a trend can be inferred from (17). Hence, we hereafter suppose the main current speed is distinguishable based on the tension measurements when a group of mooring lines are exposed to a specific current profile.

However, the current profile type is not easily distinguished with merely mooring tension units. For example, the tension variances due to uniform current $v = 0.5$ and linearly sheared $v = 1$ are almost the same. Then, the riser end angles are employed to detect the influence of the different current profiles. We propose an algorithm that can detect the depth-dependent 2D current profiles, but which are not limited into the few types given in Table 1. The static simulation results are presented in Fig. 5. Besides that, a larger current speed near the water surface increases the top end angle, and vise versa. Since the riser end angles are influenced by the current profile, these are supplemented to the tension measurements.

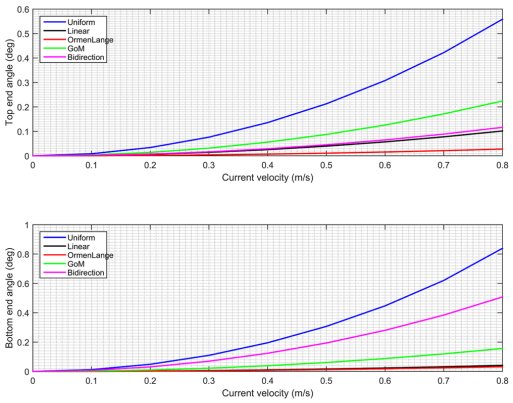


Fig. 5. End angles of a tensioned riser in five specific current profiles.

### 3.6 *Influence of vessel motion*

The tension measurements are influenced by the loading situation, the sensor noise and bias, and the wave-induced motion, being the surge, sway, heave, and pitch motions. For a given environmental load, such as a steady current profile, a moored floating structure has an equilibrium position $[x_{eq}\ y_{eq}\ z_{eq}]^\top$. With the first-order wave-induced loads, the moored vessel keeps oscillating around the equilibrium position. The magnitude of the wave-induced motion is not significant compared to the length of the cables. Therefore, we assume the tension variance is linearly dependent on the motion.

Fig. 6 presents the static influence of motion to a cable in 3D. In the simulation, the anchor lays 1950 meters away from the vessel in the heading direction. We notice that the tension variance due to the vessel's motion depends neither on the current profile type nor on the current velocity. The tension variance is, however, proportional to the surge and heave motion. We also notice that the tension variance aroused by this mooring line caused by the sway motion has an asymmetric property, but is not linearly proportional to the motion magnitude. This is because the elongation of the cable's projection on the seafloor is $\Delta X = \sqrt{(x-x_a)^2+(y-y_a)^2} - X_0$, which is nonlinear. However, the magnitude of the tension variance caused by the sway motion is much smaller than that caused by the surge motion. The tension variance is assumed to be an $\mathscr{L}_2$ norm of the tension variance vector, such that

$$\Delta T_j(t) = |\mathscr{K}_j \boldsymbol{R}^\top(\psi_m^j)\Delta\boldsymbol{p}(t)|, \tag{18}$$

where $\mathscr{K}_j = diag\{\frac{\partial T_j}{\partial x}|_{x=x_{eq}}, \frac{\partial T_j}{\partial y}|_{y=y_{eq}}, \frac{\partial T_j}{\partial z}|_{z=z_{eq}}\} \in \mathbb{R}^{3\times 3}$ and $\Delta\boldsymbol{p}(t) = \boldsymbol{p} - \boldsymbol{p}_{eq} = [x(t)-x_{eq}, y(t)-y_{eq}, z(t)-z_{eq}]^\top$.

When the vessel oscillates around the equilibrium position, the mean position variance is zero, such that $\lim_{\Delta t\to\infty} \int_t^{t+\Delta t} \boldsymbol{p}(\tau)d\tau = \boldsymbol{p}_{eq}$. Then we disregard the asymmetric property in the sway motion, and assume the mean value of the tension variance caused by motion is zero. Note that this assumption is based on the fact that the magnitude of the sway motion is not significantly larger than the surge. The estimation error can be lessened if we employ the GPS measurement as a feedforward

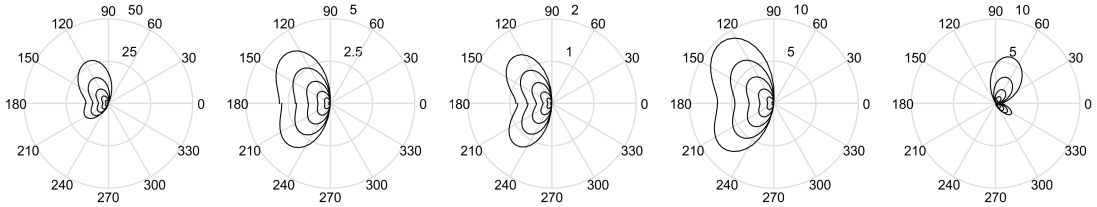

Fig. 4. Tension variance for different current profiles and orientations when $\psi_m = 0$. From the left to the right side, the current profiles are uniform, linear, Ormen Range, GoM, and bidirectional, respectively. From inside to outside in the polar plots, the current velocities are 0.2, 0.4, 0.6, 0.8, 1.0, and 1.2 m/s.

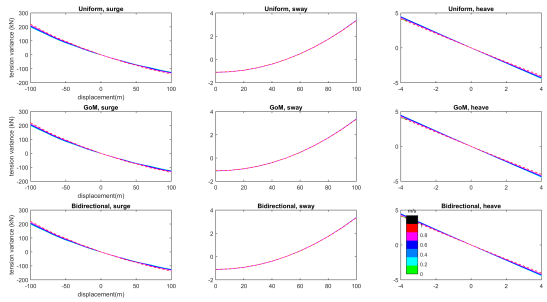


Fig. 6. Tension variance due to current velocity and vessel motion in different current profiles.

information. However, such alteration will also increase the complexity of the information matrices, and, consequently, the computational time.

Being also a slender body, a riser shares the same properties as a mooring line and oscillates with the surge and sway motion similarly.

## 4 Current profile estimation algorithm

Assume the loads are steady, and the COG is constant during window. It also simplifies the design to suppose the lengths of the mooring lines are unchangeable during the time window. Based on the former discussion, linearized characteristic is presented with small-magnitude oscillation around the equilibrium position. During the installation, the anchor positions are known, and the GPS and IMU units can measure the vessel position accurately. The algorithm is concluded in Algorithm 1. It will not give accurate estimation if the current profile is too complex, which is normally not realistic.

The optimization criterion is to minimize the error between the measurements and the estimation. $\bar{T}_j$ is the average tension measurement of the $j^{th}$ cable in a window. Moving average is applied to eliminate the effects of sensor noise and wave-induced motion. The length of the window obviously effects the results. A too short time window may cause inaccuracy, while a too long window will be insensitive to the whether change and slow down the detection speed.

To accelerate the computational efficiency, we calculate the initial information in the anchor-fixed frame, such that the anchors are set away from the fairleads in the corresponding $x$-axes with distance $\sqrt{(x-x_a^j)^2+(y-y_a^j)^2}$, and the current generalized orientation is $\beta_{c,j} = \beta_c - \psi_m^j$. Only the data with the range from 0 to $\frac{\pi}{2}$ is necessary to be computed a priori due to symmetry, such that if $\beta_{c,j_1} + \beta_{c,j_2} = 2\pi \Rightarrow T_{j_1}(\mathscr{V}_c) = T_{j_2}(\mathscr{V}_c)$, and if $\beta_{c,j_1} + \beta_{c,j_2} = \pi \Rightarrow T_{j_1}(\mathscr{V}_c) = T_{j_2}(-\mathscr{V}_c)$. These strategies will help the computer ro use the same group of priori data, regardless of the locations and orientations of the cables.

**Algorithm 1** On-site current profile estimation.

**Inputs:** $\mathscr{T}(t)$, $T_{top}$, $\vartheta(t)$, $\boldsymbol{p}(t)$.
**Initialize:** $\{T_j^*(|\boldsymbol{p} - \boldsymbol{p}_a^j|, \mathscr{D}, \mathscr{V}_c, \beta_c) | j = 1, \cdots, m\}$, $\vartheta^*(T_{top}, |\boldsymbol{p} - \boldsymbol{p}_1^r|, \mathscr{D}, \mathscr{V}_c, \beta_c)$, $\boldsymbol{\Phi}_m$.
**Outputs:** $\mathscr{D}$, $\mathscr{V}_c^*$, $\beta_c^*$.
**Governing equation:**

$$\begin{aligned} \min_{\mathscr{D},\mathscr{V}_c,\beta_c} \quad & \sum_{j=1}^{m} \alpha_T \left(\bar{T}_j - T_j^*\right)^2 + \sum_{\iota\in\{t,b\}} \alpha_\theta (\bar{\theta}_\iota - \theta_\iota^*)^2 \\ s.t. \quad & |v_c(D^p)| \preceq v_{c,max}(D^p) \\ & |\beta_c| \preceq \pi \end{aligned} \tag{19}$$

**Steps:**
(1) Calculate and store the priori information, i.e., $T_j^*$ and $\vartheta^*$;
(2) Collect the sensor data $T_j(t)$ and $\vartheta(t)$, and compute $\bar{T}_j$ and $\bar{\vartheta}$ with moving average through a window function, i.e., $\bar{T}_j = \frac{1}{\Delta t}\int_{t_0}^{t_0+\Delta t} T_j(\tau)d\tau$ and $\bar{\vartheta} = \frac{1}{\Delta t}\int_{t_0}^{t_0+\Delta t} \vartheta(\tau)d\tau$;
(3) Minimize the governing equation and receive the estimation $\mathscr{D}$, $\mathscr{V}_c^*$, and $\beta_c^*$.

It is formulated as

$$T_j^*(\cdot,\cdot,\mathscr{V}_c,\beta_{c,j}) = \begin{cases} T_j^*(\cdot,\cdot,\mathscr{V}_c,|\beta_{c,j}|), & \beta_{c,j} \in [-\frac{\pi}{2},\frac{\pi}{2}], \\ T_j^*(\cdot,\cdot,-\mathscr{V}_c,\pi-|\beta_{c,j}|), & \beta_{c,j} \in [-\pi,-\frac{\pi}{2}) \cup (\frac{\pi}{2},\pi]. \end{cases} \tag{20}$$

When the surface current speed and current direction can be detected from onboard instruments or external observation, the accuracy can be enhanced. As $O(\sum_{j=1}^m \left(\bar{T}_j - T_j^*\right)^2)$ is much larger than the $O(\sum_{\iota\in\{t,b\}}(\bar{\theta}_\iota - \theta_\iota^*)^2)$, the coefficient $\alpha_\theta$ is much larger than $\alpha_T$. Normalization is another option.

## 5 Simulation

The simulation was conducted in the MATLAB and Simulink environment, with the MSS toolbox (MSS. Marine Systems Simulator, 2010). With the advancement of the computational capacity of personal computer in the last decade, the FEM model code no longer occupies too much hardware resources. Therefore, the FEM models have been reprogrammed in Simulink S-functions for simplification (Ren, 2015). The key structural parameters are tabulated in Table 2 and Table 3.

Table 2. Mooring line dimensions.

| Principle Dimension | Values |
|---|---|
| Dens. of ambient water $\rho_w(kg/m^3)$ | 1025 |
| Length of the cable $L_m(m)$ | 2250 |
| Elastic modulus $E_m(Pa)$ | $4.5757 \times 10^{10}$ |
| Cable cross section area $A_m(m^2)$ | 0.005 |
| Cable diameter $d_m(m)$ | 0.08 |
| Max strain $\varepsilon$ | 0.005 |

Table 3. Riser main particulars.

| Dynamic parameters | Values |
|---|---|
| Damping coefficient $\alpha_2$ | 0.0477 |
| External diameter $D_{ex}$ (m) | 0.3 |
| Internal diameter $D_{int}$ (m) | 0.25 |
| Drag coefficient $C_D$ | 1.0 |
| Mass coefficient $C_M$ | 2.2 |
| Modulus of elasticity $E$ (Gpa) | 206 |
| Riser length (m) | 1000 |
| Top tension (kN) | 2700 |
| Density of steel $\rho_s$ ($kgm^3$) | 7850 |
| Density of water $\rho_w$ ($kgm^3$) | 1025 |
| Density of internal fluid $\rho_f$ ($kgm^3$) | 800 |

In this simulation, waves are generated based on the ITTC spectrum, and the current profile is given a particular. The significant wave height is 2.5 meters. The vessel moves around an equilibrium position by a PID-type DP controller (Ren et al., 2015a). The vessel is heading the waves while moored with 8 mooring cables evenly distributed with 45 deg intervals. We define a set of current profiles which contain three different depths, i.e., $p = 3$. The first and the third depth are at the free water surface and seafloor, respectively, i.e., $D_1 = 0\ m$ and $D_3 = D$. As the current profile changes more rapidly near the surface region, the second discrete point is chosen closer to surface; hence, we apply $D_2 = 300$ m. When a large number of $p$ is chosen, the simulation time grows tremendously. The accuracy may lessen if there are not enough mooring lines to provide tension information. Priori information is generated based on the set of current profiles. We trained it with a 3 deg interval in the current direction. The current speed ranges from $-1$ to 1 $m/s$, with a 0.1 $m/s$ interval.

Fig. 7 shows the current profile estimation performance when the current profile distributes corresponding to the priori depth. The most obvious reason for the error has been discussed in Section 3.6. The solution here is to set a threshold with a small positive constant $\varepsilon$ to find the value that ensures the governing equation in the ball $g(T_j^*) \leq g(\bar{T}_j + \varepsilon)$. Then we can find that the other values will not worsen the solution. This is similar to the Perado solution in the multi-objective optimization. The selection of the coefficients $\alpha_T$ and $\alpha_\theta$ is not very sensitive to the final estimation.

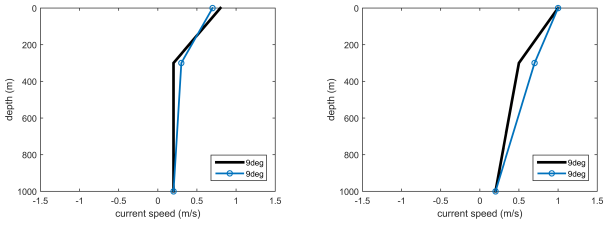


Fig. 7. The black line is the real current profile, while the blue line is the estimated profile. The estimated direction is presented in the legend.

When the current is not changed with the specific set of water depths, i.e., $D_1$, $D_2$, and $D_3$, it will be more difficult to find the best solution with the priori information. Fig. 8 are the results in this scenario. The estimated current profiles are close to their real situation. The error of the estimated and the real current direction is limited. Hence, the estimation is accepted.

## 6 Conclusion and future works

The current profile estimation is crucial to marine operations. Regular measuring methods may be expensive. Hence, this paper has proposed a 2D depth-dependent current profile estimation algorithm for a moored floating vessel based on typical existing instrumentation.

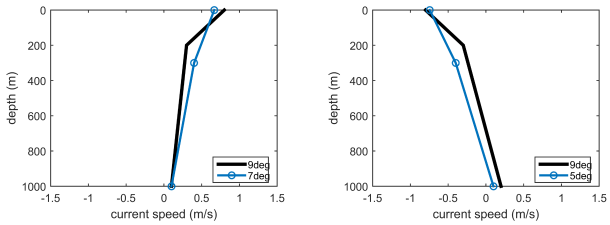


Fig. 8. The black line is the real current profile, while the blue line is the estimated profile. The estimated direction is presented in the legend.

The availability has been discussed through static analysis. The possible influences from the current profile and the vessel motion were investigated. It is a tradeoff between computation speed and estimation accuracy. A simulation study was conducted to verify the algorithm. The simulation results showed the proposed algorithm can approximately estimate the current profile. Some more sophisticated methods may be included to improve the robustness and accuracy.

In this paper, some simplifying assumptions were made. For example, the mooring line tension will not be perfect after long-term operation due to growth of marine organisms and algae, as well as the corrosion. In addition, vortex shedding is a crucial issue neglected here. More robust and adaptive current profile estimation approaches are left for future researches.

## References


Aamo, O. and Fossen, T. (2001). Finite element modelling of moored vessels. *Mathematical and Computer Modelling of Dynamical Systems*, 7(1), 47–75.

Antonelli, G., Fossen, T.I., and Yoerger, D.R. (2008). Underwater robotics. In *Springer handbook of robotics*, 987–1008. Springer.

Faltinsen, O.M. (1993). *Sea loads on ships and offshore structures*. Cambridge ocean technology series. Cambridge University Press.

Fossen, T.I. (2011). *Handbook of marine craft hydrodynamics and motion control*. John Wiley & Sons.

Gao, Z. and Moan, T. (2007). Fatigue damage induced by nongaussian bimodal wave loading in mooring lines. *Applied Ocean Research*, 29(1), 45–54.

Leira, B.J., Blanke, M., and Fang, S. (2011). Vertical position control for top tensioned riser with active heave compensator. *American Society of Mechanical Engineers*, 549–558.

Lekkas, A. and Fossen, T. (2014). Trajectory tracking and ocean current estimation for marine underactuated vehicles. In *Control Applications (CCA), 2014 IEEE Conference on*, 905–910.

MSS. Marine Systems Simulator (2010). Viewed 30.10.2014. URL `http://www.marinecontrol.org`.

Nielsen, U.D. and Jensen, J.J. (2011). A novel approach for navigational guidance of ships using onboard monitoring systems. *Ocean Engineering*, 38(23), 444 – 455.

Ren, Z. (2015). *Fault-Tolerant Control of Thruster-Assisted Position Mooring System*. Master's thesis, Norwegian University of Science and Technology, Trondheim, Norway.

Ren, Z. and Skjetne, R. (2016). A tension-based position reference solution to tapm with uncertain anchor positions. *IFAC-PapersOnLine*.

Ren, Z., Skjetne, R., and Hassani, V. (2015a). Supervisory control of line breakage for thruster-assisted position mooring system. *IFAC-PapersOnLine*, 48(16), 235–240.

Ren, Z., Skjetne, R., and Kjerstad, Ø.K. (2015b). A tension-based position estimation approach for moored marine vessels. *IFAC-PapersOnLine*, 48(16), 248–253.

Rustad, A.M. (2007). *Modeling and control of top tensioned risers*. Fakultet for ingenirvitenskap og teknologi.

Sørensen, A.J. (2012). Marine control systems propulsion and motion control of ships and ocean structures lecture notes.